EES Catalysis

PAPER

View Article Online
View Journal

Check for updates

Cite this: DOI: 10.1039/d6ey00013d

# Highly selective photothermal $CO_2$ hydrogenation to $C_2^+$ hydrocarbons over Mn-modified K–Fe catalysts

Xinhuilan Wang, Alejandra Rendón-Patiño, Diego Mateo * and Jorge Gascon *

Received 15th January 2026,
Accepted 10th February 2026

DOI: 10.1039/d6ey00013d

rsc.li/eescatalysis

Efficient and selective $CO_2$ hydrogenation pathways are pivotal for tackling climate change while enabling sustainable energy solutions. Herein, we report a series of potassium-promoted $Fe_xMn_y$ catalysts for the photothermal hydrogenation of $CO_2$ to $C_2^+$ hydrocarbons under mild reaction conditions. By tuning the Fe/Mn ratio, we identify K–$Fe_{10}Mn_1$ as the optimal composition, exhibiting a remarkable $C_2^+$ selectivity of 79.2% and a $C_{2\text{-}5}$ hydrocarbon yield of 4.8 mmol $g^{-1}$ $h^{-1}$ at 250 °C and 20 bar, under 4 W $cm^{-2}$ light irradiation. This catalyst also exhibited the lowest CO selectivity (24.1%) and the highest chain-growth probability ($\alpha$ = 0.64) among the series. In contrast, detailed characterization revealed that excessive Mn leads to over-stabilization of $Fe_1Mn_{1-x}O$ species, diminishing the availability of active $Fe_5C_2$ species and reducing C–C coupling efficiency. Mechanistic studies, including *in situ* DRIFTS, demonstrate that non-thermal effects dominate the reaction pathway, with light irradiation accelerating the generation of key intermediates without altering the intrinsic mechanism. These findings provide fundamental insights into the structure–activity relationship of K–FeMn systems and offer a promising route for solar-driven $CO_2$-to-hydrocarbon conversion under industrially relevant conditions.

Open Access Article. Published on 16 February 2026. Downloaded on 2/25/2026 3:21:28 AM.
This article is licensed under a Creative Commons Attribution 3.0 Unported Licence.

**Broader context**

The sustainable transformation of carbon dioxide into energy-rich hydrocarbons represents a cornerstone challenge in achieving a circular carbon economy. Traditional thermal $CO_2$ hydrogenation requires high temperatures and pressures, leading to significant energy consumption and limited selectivity toward multi-carbon products. Harnessing solar energy to drive this reaction efficiently under mild conditions would constitute a major step forward in carbon utilization. In this work, we introduce a family of Mn-modified K–Fe catalysts capable of converting $CO_2$ to $C_2^+$ hydrocarbons with unprecedented selectivity under photothermal conditions. By rationally tuning the Fe/Mn ratio, we demonstrate that optimal metal synergy enhances C–C coupling and hydrocarbon chain growth while suppressing unwanted CO formation. Mechanistic and *in situ* spectroscopic studies reveal that light-induced non-thermal effects accelerate key surface reactions without altering the fundamental Fischer–Tropsch pathway. These findings offer mechanistic insight into how photothermal catalysis can overcome the selectivity and efficiency limitations of conventional $CO_2$ hydrogenation. Beyond its immediate catalytic implications, this work provides design principles for solar-driven $CO_2$ conversion processes that could enable cleaner, more energy-efficient production of sustainable fuels and chemicals.

## 1. Introduction

The global energy crisis has become a significant challenge in addressing the increasing demand for energy and mitigating the environmental impacts associated with fossil fuel consumption.[1,2] Fossil fuels, such as coal, oil, and natural gas, continue to dominate the global energy supply due to their high energy density and established infrastructure.[3] However, the uneven distribution of fossil fuel reserves across the world exacerbates energy access disparities, particularly in developing regions.[4] In addition, the combustion of fossil fuels is a major contributor to $CO_2$ emissions, which significantly accelerates climate change and leads to adverse environmental consequences, including rising global temperatures, extreme weather events, and sea-level rise.[5,6]

With escalating $CO_2$ emissions and a growing global energy crisis, carbon capture, utilization, and storage (CCUS) stands at the forefront of strategies to curb carbon accumulation and advance energy sustainability.[7,8] In this regard, the conversion of $CO_2$ into valuable chemicals such as carbon monoxide,[9,10] methane,[11,12] methanol,[13–15] and hydrocarbon,[16,17] offers a promising approach not only to mitigate $CO_2$ levels but also to generate high value-added fuels and chemicals. In particular, the conversion of $CO_2$ into hydrocarbons through the $CO_2$-

*Advanced Catalytic Materials (ACM), KAUST Catalysis Platform, King Abdullah University of Science and Technology (KAUST), Thuwal 23955-6900, Saudi Arabia. E-mail: diego.mateo@kaust.edu.sa, jorge.gascon@kaust.edu.sa*

Open Access Article. Published on 16 February 2026. Downloaded on 2/25/2026 3:21:28 AM. This article is licensed under a Creative Commons Attribution 3.0 Unported Licence.

based Fischer–Tropsch synthesis ($CO_2$-FTS) presents a pathway to close the carbon loop, addressing both environmental concerns and the growing demand for energy and chemical feedstocks. Consequently, the development of energy-efficient and selective $CO_2$ conversion technologies has proved essential to achieve a sustainable energy future.

In this context, solar energy is considered a clean and abundant resource with the potential to fundamentally transform $CO_2$ conversion technologies without relying on fossil fuels.[18,19] In fact, when it comes to heterogeneous catalysis, beyond serving as a renewable heat source, solar irradiation has emerged as a key factor to accelerating catalytic processes, modifying the reaction kinetics, and improving the reaction efficiency through photon-induced electronic excitation.[20–22] By simultaneously harnessing light and heat from solar radiation, photothermal catalysis can integrate thermal activation with photon-induced effects, enabling efficient solar-driven chemical transformations[23–25] with lower energy barriers, particularly in $CO_2$ hydrogenation.[26,27] Nevertheless, although the photothermal $CO_2$ hydrogenation toward hydrocarbons has been previously investigated, most studies remain limited to ambient pressure conditions,[28–30] mainly due to constraints in reactor configuration, heat management and/or photon collection upon increasing the operating pressure. Therefore, the combination of thermal and photochemical effects under industrially relevant $CO_2$-FTS conditions remains largely unexplored.

Fe-based catalysts, comprising magnetite (*e.g.*, $Fe_3O_4$) and carbides (*e.g.*, $Fe_5C_2$ and $Fe_2C$), are widely used in $CO_2$-FTS, where iron oxides facilitate CO formation *via* RWGS and carbides enable C–C coupling.[31–34] However, unpromoted Fe catalysts often suffer from deactivation and low hydrocarbon selectivity due to phase instability and methanation.[35–38] The incorporation of promoters has proven to be one of the most effective strategies for enhancing the activity and selectivity of Fe-based catalysts.[36] For instance, alkali promoters (*e.g.*, K, Na, Cs) could effectively enhance catalytic activity and hydrocarbon selectivity by modulating the electronic structure of iron phases and suppressing undesired hydrogenation pathways.[39–42]

Transition metals, including Co,[43,44] Cu,[45] Mn,[32,46–48] and Zn,[34,49] significantly influence the electronic properties of Fe-based catalysts in the $CO_2$-FTS reaction. Among these, Mn has attracted considerable attention due to its cost-effectiveness and its ability to enhance hydrocarbon selectivity.[46,47] Recently, Kondratenko and colleagues reported that a Mn-modulated Fe-based catalyst enhanced hydrocarbon selectivity in the $CO_2$-FTS reaction.[47] They found that an *in situ* MnO-containing layer formed on the surface of iron carbide, which reduced hydrogenation activity, thereby inhibiting methanation and promoting hydrocarbon formation. However, previous studies have shown that Mn could enhance the dispersion of $FeO_x$ catalysts, while strong Fe-Mn interactions stabilize the $Fe_1Mn_{1-x}O$ phase, suppressing the formation of active $FeC_x$ species.[50,51] Overall, an appropriate Fe/Mn ratio plays a crucial role in governing the $CO_2$-FTS reaction.

Motivated by the challenges and opportunities outlined above, we investigate potassium (K)-promoted $Fe_xMn_y$ catalysts with varying Fe/Mn ratios for photothermal $CO_2$ hydrogenation, targeting the production of $C_2^+$ hydrocarbons in a continuous flow reactor operated under industrially relevant conditions (250 °C, 20 bar). Structure–activity relationship optimization reveals that the K-promoted $Fe_{10}Mn_1$ catalyst achieves the lowest CO selectivity (24.1%) and the highest chain growth probability ($\alpha$ = 0.64) among the tested K–$Fe_xMn_y$ catalysts, indicating an optimal Fe/Mn ratio. To the best of our knowledge, this catalyst delivers a $C_2^+$ hydrocarbon selectivity of 79.2% at 20 bar, with a $C_{2-5}$ hydrocarbon yield of 4.8 mmol $g^{-1}$ $h^{-1}$, representing state-of-the-art performance for photothermal $CO_2$ hydrogenation. Mechanistic investigations suggest that non-thermal effects serve as the primary driving force for photothermal $CO_2$ hydrogenation. Complementary *in situ* DRIFTS measurements further confirm that light irradiation accelerates the formation of key intermediates, thereby enhancing overall catalytic performance.

## 2. Catalysts preparation

A series of $Fe_xMn_y$ catalysts, with different Fe/Mn atomic ratios, was prepared *via* the co-precipitation method using iron(III) nitrate nonahydrate ($Fe(NO_3)_3{\cdot}9H_2O$) and manganese(II) nitrate tetrahydrate ($Mn(NO_3)_2{\cdot}4H_2O$) as the metal precursors. Typically, appropriate amounts of $Fe(NO_3)_3{\cdot}9H_2O$ and $Mn(NO_3)_2{\cdot}4H_2O$ were dissolved in deionized water (100 mL) for a total molar concentration of $Fe^{3+}$ and $Mn^{2+}$ of 0.4 mol $L^{-1}$. Each mass of $Fe(NO_3)_3{\cdot}9H_2O$ and $Mn(NO_3)_2{\cdot}4H_2O$ was determined by the atomic ratio of Fe to Mn (10/1, 7/1, 5/1, 4/1, 3/1, and 2/1). The mixture was stirred at room temperature for 1 h. Then, ammonia solution ($NH_4OH$; Sigma Aldrich, 25% $NH_3$ in $H_2O$) was added dropwise into the above solution under stirring until the pH value reached 10. The suspension was aged for 2 h, filtered and washed until a neutral pH value was achieved. The obtained samples were dried at 80 °C overnight. Subsequently, the dried precursor was impregnated with a solution of potassium nitrate ($KNO_3$) in water by wetness impregnation to obtain 2 wt%. The K-promoted samples were first dried at 100 °C for 1.5 h and then calcined at 450 °C with a heating rate of 3 °C $min^{-1}$ for 3 h. They were named K–$Fe_xMn_y$, where $x/y$ stands for the atomic ratio of Fe to Mn. The catalyst without Mn was also prepared using only $Fe(NO_3)_3{\cdot}9H_2O$ while other preparation conditions were kept the same, named as K–Fe.

Lastly, the calcined sample was reduced in a flow of 6 vol% $H_2$/Ar at 400 °C for 2 hours, and then passivated in a flow of 5 vol% $O_2/N_2$ at room temperature for 1 hour. Before the catalytic testing, the reduced samples were kept in a vial with a seal inside a glove box to prevent further oxidation.

## 3. Photothermal $CO_2$ hydrogenation reaction

The photo-thermal $CO_2$ hydrogenation reaction was evaluated using a commercial flow reactor equipped with a quartz window (Harrick, HVC-MRA-5) and a 300 W Xe lamp (PE300BFA, Perfectlight) as the irradiation source. In a typical experiment,

 © 2026 The Author(s). Published by the Royal Society of Chemistry

Open Access Article. Published on 16 February 2026. Downloaded on 2/25/2026 3:21:28 AM.
This article is licensed under a Creative Commons Attribution 3.0 Unported Licence.

50 mg of pre-reduced catalyst was loaded on the reactor. A thermocouple to monitor the temperature was located *ca.* 1 mm below the catalyst's surface. The reaction gas mixture ($H_2/CO_2$ ratio of 4 : 1) was introduced through the reactor with a total flow rate of 10 mL $min^{-1}$ (GSHV = 12 000 mL $h^{-1}$ $g^{-1}$). Nitrogen was used as an internal standard. The evolved gases were analyzed by a gas compact chromatograph (CompactGC, Thermo Fisher) directly connected to the reactor outlet (Fig. S11).

$CO_2$ conversion was calculated by the following formula (eqn (1)):

$$X_{CO_2}(\%) = 100 \times \left(1 - \frac{C_{CO_2,out} \times C_{N_2,in}}{C_{CO_2,in} \times C_{N_2,out}}\right) \quad (1)$$

The CO selectivity ($S_{CO}$) was given as formula (eqn (2)):

$$S_{CO}\ (\%) = 100 \times \left(\frac{C_{CO}}{C_{CO} + \sum_{i=1}^{n} C_{i\,hydrocarbon} \times i}\right) \quad (2)$$

The selectivity towards $C_i$ hydrocarbons ($S_{C_{i\,hydrocarbon}}$) was given as formula (eqn (3)):

$$S_{C_{i\,hydrocarbon}}(\%) = 100 \times \left(\frac{C_{i\,hydrocarbon} \times i}{C_{CO} + \sum_{i=1}^{n} C_{i\,hydrocarbon} \times i}\right) \quad (3)$$

## 4. Results and discussion

Potassium-promoted iron-based catalysts with a range of Fe/Mn atomic ratios (denoted as K–$Fe_xMn_y$; Table S1) were prepared using a co-precipitation method. Powder X-ray diffraction (PXRD) patterns of the calcined samples (Fig. S1) demonstrated that α-$Fe_2O_3$ (hematite) was the only crystalline phase observed in catalysts with Fe/Mn ratios between 10 : 1 (K–$Fe_{10}Mn_1$) and 5 : 1 (K–$Fe_5Mn_1$). No additional peaks corresponding to potassium are observed in the PXRD patterns, indicating its uniform dispersion within the K–$Fe_xMn_y$ catalysts. Notably, increasing the Mn content led to a pronounced decrease in both crystallinity and crystal size of $Fe_2O_3$ (Table S2). When the Fe/Mn ratio dropped below 5 : 1, Fe species became predominantly X-ray amorphous. This behavior highlights that Mn as a structural promoter could effectively hinder crystallite growth and promote Fe dispersion.[46] Such structural modification led to a pronounced enhancement in specific surface area. Moreover, the UV-Vis-NIR absorption spectra of K–$Fe_xMn_y$ oxides show that the monometallic K–Fe catalyst exhibits two distinct absorption bands at 345 and 530 nm, characteristic of α-$Fe_2O_3$. With increasing Mn content, both bands progressively weaken, further indicating a decrease in crystallinity (Fig. S2). As shown in Table S3 and Fig. S3, the BET surface area increased significantly from 26 $m^2$ $g^{-1}$ for K–Fe to 115 $m^2$ $g^{-1}$ for K–$Fe_{10}Mn_1$, and further rose to 287 $m^2$ $g^{-1}$ at a Fe/Mn ratio of 7 : 1. However, a subsequent increase in Mn content (Fe/Mn = 2 : 1) resulted in a reduction of surface area to 172 $m^2$ $g^{-1}$.

The reducibility of the K–$Fe_xMn_y$ catalysts was investigated using $H_2$ temperature-programmed reduction ($H_2$-TPR, Fig. S4). For K–Fe, two major hydrogen consumption peaks were observed: The first at 422 °C, corresponding to the reduction of $Fe_2O_3$ to $Fe_3O_4$, and the second at around 595 °C, attributed to the further reduction to FeO/$Fe^0$.[32,46] In contrast, the K–$Fe_xMn_y$ catalysts displayed more complex reduction behavior. A low-temperature peak near 270 °C was assigned to the reduction of $MnO_2$ to $Mn_2O_3$,[52] while a broader peak between 350–370 °C was associated with overlapping reduction events of $Fe_2O_3$ → $Fe_3O_4$ and $Mn_2O_3$ → $Mn_3O_4$.[50,53] A subsequent peak at approximately 500 °C was attributed to the reduction of $Mn_3O_4$ to MnO. Interestingly, the incorporation of Mn lowered the temperature required for $Fe_3O_4$ formation, suggesting the formation of a $Fe_1Mn_{1-x}O$ solid solution.[47,54] However, the subsequent reduction of $Fe_3O_4$ to metallic Fe was significantly hindered in Mn-containing samples, with reduction temperatures exceeding 600 °C. This shift implies that the $Fe_3O_4$/$Fe_1Mn_{1-x}O$ phase becomes increasingly resistant to reduction as Mn content increases, potentially stabilizing intermediate mixed oxide phases.[47]

Based on $H_2$-TPR analysis, all catalysts were pre-reduced at 400 °C under a flow of 6 vol% $H_2$/Ar for 2 h and subsequently passivated under 5 vol% $O_2/N_2$ at room temperature for 1 h. The phase composition of the reduced catalysts was analyzed by PXRD (Fig. S5). The reduced monometallic K–Fe sample exhibited a mixture of $Fe_3O_4$ and metallic Fe. In contrast, the reduced K–$Fe_xMn_y$ catalysts showed the emergence of a new diffraction peak at 41.6°, alongside reflections attributed to $Fe_1Mn_{1-x}O$. This peak progressively shifted to lower 2$\theta$ angles with increasing Mn content. Phase identification revealed that the peak corresponds to $Fe_{0.899}Mn_{0.101}O$ (ICSD-60684) in K–$Fe_{10}Mn_1$ and evolves to $Fe_{0.497}Mn_{0.503}O$ (ICSD-60687) in K–$Fe_2Mn_1$. Moreover, the intensity of metallic Fe diminished with increasing Mn content and disappeared entirely in the K–$Fe_2Mn_1$ sample. Quantitative XRD analysis confirmed a decrease in metallic Fe and a concurrent increase in $Fe_1Mn_{1-x}O$ with higher Mn loading (Fig. S6 and Table S4). These findings are consistent with $H_2$-TPR results, reinforcing that the incorporation of Mn could stabilize Fe-containing mixed oxides against full reduction to metallic Fe. Therefore, a pre-reduction temperature of 400 °C was selected to predominantly form $Fe_3O_4$ and Fe-Mn mixed oxides, which are active for the RWGS reaction and can subsequently undergo *in situ* carburization to generate iron carbide species under reaction conditions. There carbide phases are widely recognized as the active phase for C–C coupling and $C_2^+$ hydrocarbon formation.[33,55] Moreover, as shown in Fig. S7, the UV-Vis-NIR absorption spectra of the reduced K–$Fe_xMn_y$ catalysts show the complete disappearance of the α-$Fe_2O_3$ absorption bands compared to the oxidized samples. All reduced catalysts exhibit broad, continuous absorption across the visible to NIR region, indicative of excellent light-harvesting capability and suggesting strong potential for enhanced photothermal and photochemical activity.

Transmission electron microscopy (TEM) analysis of the reduced K–$Fe_{10}Mn_1$ catalyst (Fig. S8) revealed well-defined

Open Access Article. Published on 16 February 2026. Downloaded on 2/25/2026 3:21:28 AM.
This article is licensed under a Creative Commons Attribution 3.0 Unported Licence.

lattice fringes with spacings of 0.249, 0.296, and 0.203 nm, corresponding to the (111) plane of $Fe_1Mn_{1-x}O$, the (200) plane of $Fe_3O_4$, and the (110) plane of metallic Fe, respectively, which is consistent with the PXRD results. In addition, elemental mapping (Fig. S9 and S10) confirmed a homogeneous distribution of Mn and K throughout the reduced sample, indicating uniform incorporation of promoter elements within the catalyst matrix.

The catalytic performance and hydrocarbon product distribution for $CO_2$ hydrogenation over a series of K–$Fe_xMn_y$ catalysts were evaluated under photo-thermal conditions, using a 300 W xenon lamp (light intensity: 4 W $cm^{-2}$) with external heating at 250 °C, a total pressure of 20 bar, and a space velocity of 12 000 mL $g^{-1}$ $h^{-1}$ (Fig. S11). The $CO_2$ conversion and product selectivity reached a steady state within around 15 hours, which can be attributed to the gradual formation of active sites (Fig. S13). The $CO_2$ conversion and product selectivity were monitored over 35 h of time-on-stream (TOS) for the various K–$Fe_xMn_y$ catalysts (Fig. 1a and Fig. S14 and Table S6). As shown in Fig. 1a and Fig. S14, all catalysts exhibited comparable $CO_2$ conversions in the range of 44–50%, highlighting the high activity of K-promoted FeMn systems for photo-thermal $CO_2$ hydrogenation. Notably, the CO selectivity decreased from 37.3% to 24.1% as the Mn content decreased from Fe/Mn = 2/1 to Fe/Mn = 10/1, while the $C_2^+$ hydrocarbon selectivity correspondingly rose from 46.8% to 59.6%. This inverse trend in CO and $C_2^+$ selectivity correlates with XRD analysis of the reduced catalysts, which reveals that a higher Mn content stabilizes Fe-based oxides and promotes the formation of $Fe_1Mn_{1-x}O$ solid solutions. Such structural stabilization, arising from the low reducibility of Fe-Mn solid solutions, could reduce the amount and surface accessibility of Fe species available for carburization. Consequently, the formation of iron carbide phases under reaction conditions is suppressed, leading to an attenuation of the Fischer–Tropsch synthesis (FTS) pathway essential for hydrocarbon production. Moreover, $CO_2$-temperature-programmed desorption ($CO_2$-TPD) analysis (Fig. S15) revealed that an optimal Mn content acts as an effective structural promoter, enhancing $CO_2$ adsorption capacity and strengthening the interaction between $CO_2$ molecules and the catalyst surface.

The Anderson–Schulz–Flory (ASF) product distributions for the K-promoted $Fe_{10}Mn_1$ and monometallic K–Fe catalysts are shown in Fig. 1b and c. Compared to K–Fe, the K–$Fe_{10}Mn_1$ catalyst exhibited a higher chain growth probability, indicative of more efficient C–C coupling. However, further increasing the Mn content led to a decline in chain growth probability, suggesting that an optimal Fe/Mn ratio is essential for effective $CO_2$-FTS (Fig. S16 and S17). A balanced Fe/Mn composition not only enhances overall hydrocarbon productivity but also promotes the formation of longer-chain hydrocarbons.

Catalytic stability is a key point for industrial applications. As illustrated in Fig. 1d, the K–$Fe_{10}Mn_1$ catalyst exhibited

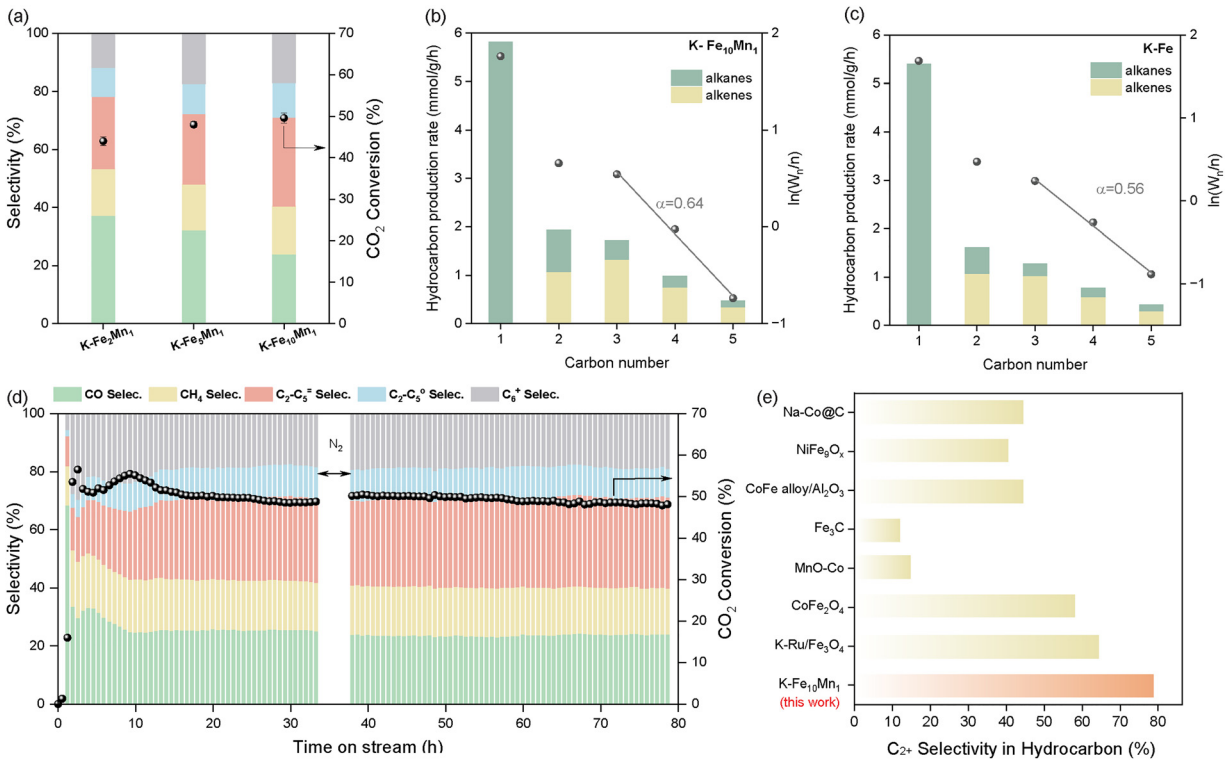


Fig. 1 Photothermal $CO_2$ hydrogenation reaction. (a) $CO_2$ conversion and product selectivity over K–$Fe_2Mn_1$, K–$Fe_5Mn_1$, and K–$Fe_{10}Mn_1$ catalysts at TOS of 35 hours. (b-c) Hydrocarbon distribution and ASF plot over K–$Fe_{10}Mn_1$ and K–Fe catalyst at TOS of 35 hours. (d) Stability test of K–$Fe_{10}Mn_1$ catalyst. Reaction conditions: GSHV = 12 000 mL $g^{-1}$ $h^{-1}$, $H_2/CO_2$ = 4, P =20 bar, 4 W $cm^{-2}$ light irradiation with external heating at 250 °C. (e) Comparison of the hydrocarbon selectivity of $C_2^+$ with reported state-of-the-art catalysts in the photo-thermal $CO_2$-to-hydrocarbon reaction.

 © 2026 The Author(s). Published by the Royal Society of Chemistry

Open Access Article. Published on 16 February 2026. Downloaded on 2/25/2026 3:21:28 AM.
This article is licensed under a Creative Commons Attribution 3.0 Unported Licence.

remarkable stability over 80 h of time-on-stream (TOS) under photo-thermal conditions, maintaining consistent $CO_2$ conversion, CO selectivity, and hydrocarbon selectivity without observable degradation. Notably, steady-state performance was achieved after approximately 15 h, likely due to the gradual formation and evolution of active catalytic sites. To mitigate potential surface temperature drops caused by hydrocarbon accumulation, the feed was switched to $N_2$ after 35 h of reaction for a 3 h purge under identical conditions, effectively removing adsorbed hydrocarbon species from the catalyst surface. These results underscore the structural robustness of the catalyst and its strong potential for long-term solar-driven $CO_2$ hydrogenation reaction.

In comparison with previously developed photothermal catalysts in the $CO_2$ hydrogenation reaction, the K-promoted $Fe_{10}Mn_1$ exhibited exceptional performance, achieving a $C_2^+$

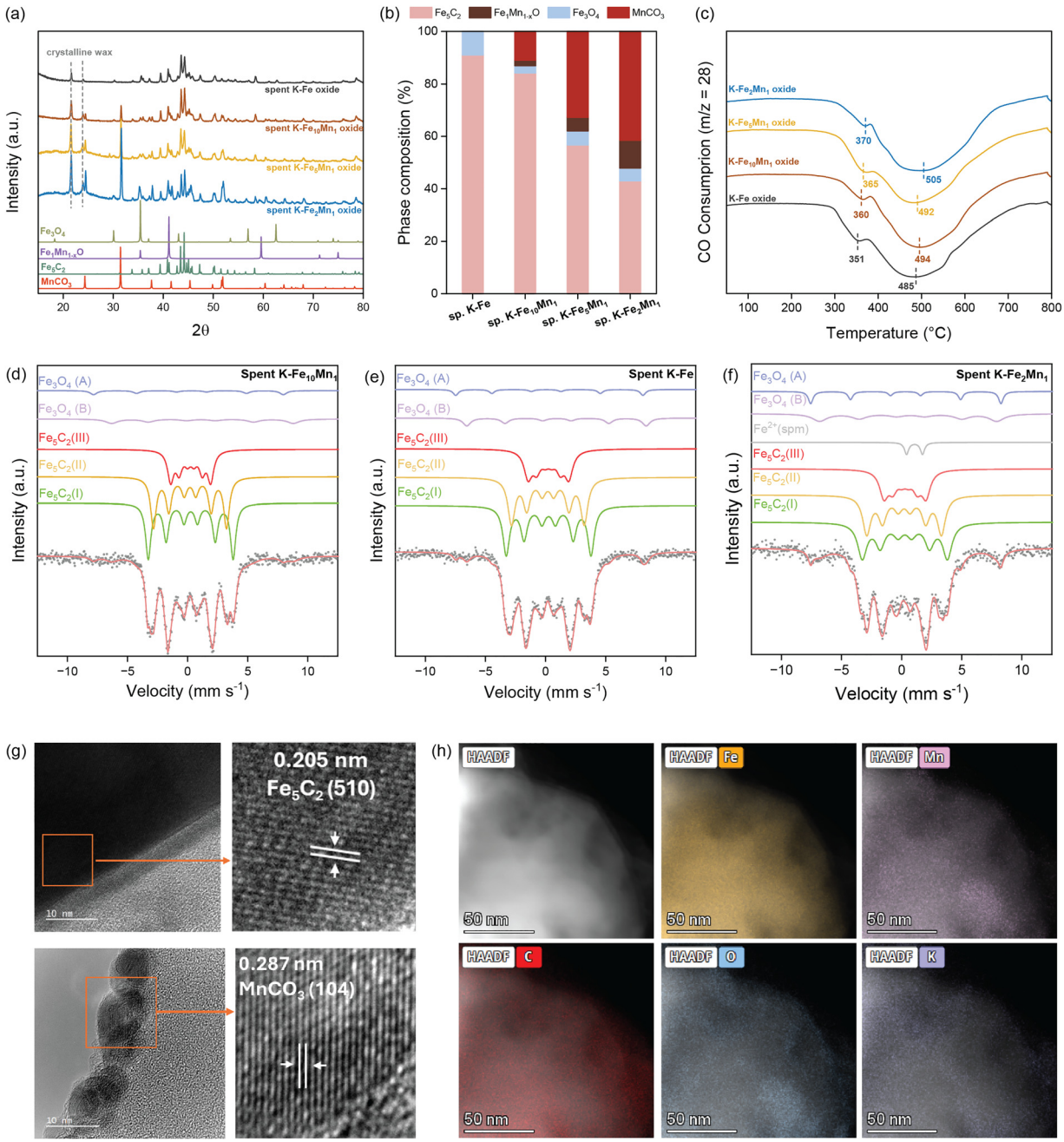


Fig. 2 Spent catalyst characterizations. (a) PXRD patterns for spent K–$Fe_xMn_y$/K–Fe catalysts after photo-thermal $CO_2$ hydrogenation reaction after TOS = 35 hours at 20 bar under 4 W $cm^{-2}$ irradiation with 250 °C external heating. Simulated XRD patterns for $Fe_5C_2$, $Fe_3O_4$, $Fe_1Mn_{1-x}O$, and $MnCO_3$ are included for reference. (b) Phase composition of the spent catalysts based on the Rietveld quantitative phase analysis of their PXRD patterns. (c) CO-TPR for spent K–$Fe_xMn_y$/K–Fe catalysts. (d)–(f) Mössbauer spectra of the spent K–$Fe_{10}Mn_1$, spent K–Fe, and spent K–$Fe_2Mn_1$ catalysts. (g) TEM images and (h) STEM images with elemental mapping by EDX of spent K–$Fe_{10}Mn_1$ catalyst.

Open Access Article. Published on 16 February 2026. Downloaded on 2/25/2026 3:21:28 AM. This article is licensed under a Creative Commons Attribution 3.0 Unported Licence.

hydrocarbon selectivity of 79.2% (CO free) at 20 bar, surpassing previously reported benchmarks for photo-thermal $CO_2$-to-hydrocarbon conversion (Fig. 1e). Under these conditions, the $C_{2-5}$ hydrocarbon yield reached 4.8 mmol $g^{-1}$ $h^{-1}$, representing the highest value reported to date for photo-thermal $CO_2$ hydrogenation. (Table S10) Furthermore, relative to purely thermal catalysis, the K–$Fe_{10}Mn_1$ catalyst demonstrated outstanding photothermal $CO_2$ hydrogenation activity under mild reaction temperatures (Table S11).

To gain deeper insight into phase transformations and the role of Mn in Fe catalyst during the photo-thermal $CO_2$ hydrogenation reaction, a series of characterizations was conducted on the spent K–$Fe_xMn_y$/K–Fe catalysts after 35 h of time-on-stream. As shown in Fig. 2a and Fig. S18, PXRD analysis revealed distinct diffraction peaks corresponding to $Fe_5C_2$ (ICSD-423887) and $Fe_3O_4$ (ICSD-249047) across all K–$Fe_xMn_y$ and K–Fe catalysts. This suggests that $Fe_5C_2$ is formed *in situ* from $Fe_3O_4$ and metallic Fe during the reaction and is responsible for C–C coupling in the FTS pathway.[46,56] In contrast to the monometallic K–Fe catalyst, additional reflections assigned to $MnCO_3$ (ICSD-80867) and $Fe_1Mn_{1-x}O$ were observed in the K–$Fe_xMn_y$ samples, with increasing intensity upon higher Mn loading. TEM images of the K–$Fe_{10}Mn_1$ catalyst after the photothermal reaction (Fig. 2g) confirmed the formation of $\chi$-$Fe_5C_2$ and $MnCO_3$ phases, with lattice spacings of 0.205 nm and 0.287 nm corresponding to the (510) and (104) planes, respectively. In addition, elemental mapping (Fig. 2h) revealed a homogeneous distribution of K and Mn throughout the spent catalyst, indicating the structural stability and uniform dispersion of promoter elements under reaction conditions.

To further quantify the phase composition, Rietveld analysis of the XRD patterns was performed (Fig. 2b and Fig. S19 and Table S5). As per these analyses, there is 91% $Fe_5C_2$ and 9% $Fe_3O_4$ in the K–Fe catalyst after reaction, consistent with the classical "tandem mechanism" where $Fe_3O_4$ facilitates the RWGS reaction and $Fe_5C_2$ drives subsequent hydrocarbon formation *via* FTS.[35,57] Upon Mn incorporation, however, the fraction of $Fe_5C_2$ decreased, while $Fe_1Mn_{1-x}O$ and $MnCO_3$ increased with decreasing Fe/Mn ratio. For instance, the spent K–$Fe_2Mn_1$ catalyst contained only 43.0% $Fe_5C_2$, along with 10.6% $Fe_1Mn_{1-x}O$ and 41.4% $MnCO_3$. To further elucidate the evolution of iron species during the photothermal $CO_2$-FTS reaction, Mössbauer spectroscopy was performed (Fig. 2d–f and Fig. S20 and Table S7). As shown in Fig. 2d–f, the Mössbauer results of spent catalysts are fully consistent with the XRD analysis, confirming that iron-containing oxides are responsible for RWGS activity, whereas $Fe_5C_2$ is the exclusive carbide phase associated with hydrocarbon formation. Quantitative comparison reveals good agreement in phase composition between Mössbauer and XRD for the spent K–Fe and K–$Fe_{10}Mn_1$ catalysts. In contrast, Mössbauer spectroscopy indicates a higher fraction of $Fe_5C_2$ in spent K–$Fe_2Mn_1$ (79.8% of iron species) than that estimated from XRD (73.5% of iron species), likely due to the presence of amorphous carbide species that are not detectable by XRD (Table S8).[35] Overall, the evolution of phase composition with varying Fe/Mn ratios correlates with the observed CO selectivity. Specifically, the diminished fraction of $Fe_5C_2$ together with the increased abundance of Fe-containing oxide phases at higher Mn contents, which are active in the RWGS reaction, preferentially promotes CO formation while simultaneously suppressing C–C coupling.[47,50,51]

To assess the impact of Mn on carburization behavior, CO-temperature-programmed reduction (CO-TPR) measurements were conducted on reduced K–$Fe_xMn_y$/K–Fe catalysts (Fig. 2c). The main carburization temperatures increased from 351 °C and 485 °C for K–Fe to 370 °C and 575 °C for K–$Fe_2Mn_1$, indicating that Mn incorporation raises the carburization barrier. This behavior is associated with lower metallic Fe availability in the reduced samples, as confirmed by $H_2$-TPR results. Together, CO-TPR and $H_2$-TPR analyses reveal that the $Fe_1Mn_{1-x}O$ phase enhances the reduction resistance and suppresses Fe carburization. Overall, these findings demonstrate that Mn plays a critical role in modulating the structural evolution and catalytic function of Fe-based catalysts under photothermal $CO_2$ hydrogenation conditions. An optimal Fe/Mn ratio is thus essential not only for tuning product selectivity but also for promoting C–C coupling and hydrocarbon chain growth *via* balanced phase composition and redox behavior.

## 5. Mechanistic study

In photothermal catalysis, the interplay between photochemical and thermal effects derived from sunlight plays an important role in determining catalytic activity. Distinguishing these two contributions is therefore critical for elucidating the reaction pathway. To this end, Liu and Everitt introduced a strategy that isolates the non-thermal effects by depositing a thin layer ($\leq$ 1 mm) of $Ti_2O_3$ (a material with strong light-to-heat conversion capabilities but no intrinsic catalytic activity for $CO_2$ hydrogenation) on top of the catalyst bed (Fig. S21).[58] This configuration creates an equivalent thermal gradient under both direct and indirect illumination, enabling a controlled comparison of catalytic performance with and without photon effect access to the catalyst surface.

Using this approach, we evaluated the photothermal behavior of the K–$Fe_{10}Mn_1$ catalyst under varying light intensities. As shown in Fig. 3d, direct and indirect illumination resulted in comparable surface temperatures, confirming that the $Ti_2O_3$ overlayer provides similar thermal input while effectively blocking photon-induced excitation. The corresponding $CO_2$ conversion and product selectivity are shown in Fig. 3a and b. Notably, CO selectivity increased with decreasing light intensity, consistent with lower surface temperatures. Under direct illumination, $CO_2$ conversion exhibited a linear dependence on light intensity in the range of 2.8–4.0 W $cm^{-2}$, suggesting a dominant contribution from non-thermal effects, with a minor thermal component (Fig. 3a and Fig. S22).[23,59] In contrast, under indirect illumination, where only thermal contributions remain, the $CO_2$ conversion showed a non-linear trend, highlighting the purely thermal-driven effect in this configuration

 © 2026 The Author(s). Published by the Royal Society of Chemistry

Open Access Article. Published on 16 February 2026. Downloaded on 2/25/2026 3:21:28 AM.
This article is licensed under a Creative Commons Attribution 3.0 Unported Licence.

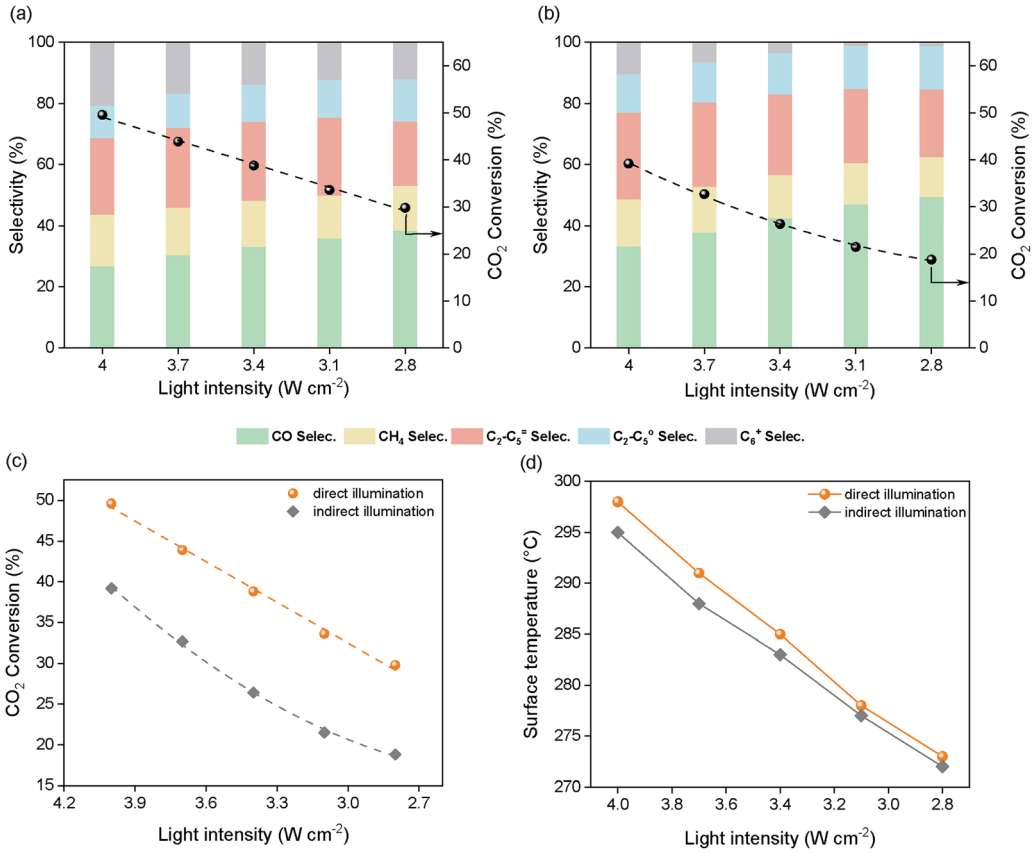


Fig. 3 Direct and indirect illumination experiments. (a) $CO_2$ conversion and product selectivity over K–$Fe_{10}Mn_1$ catalyst under direct illumination of different light intensities with 250 °C external heating. (b) $CO_2$ conversion and product selectivity over K–$Fe_{10}Mn_1$ catalyst under indirect illumination (cover $Ti_2O_3$ layer) with different light intensities at 250 °C external heating. (c) Study of the effect of light intensity on the $CO_2$ conversion over K–$Fe_{10}Mn_1$ catalyst under direct and indirect illumination. (d) Surface temperature of direct and indirect light illumination under different light intensities over K–$Fe_{10}Mn_1$. Reaction condition: GSHV = 12 000 mL $g^{-1}$ $h^{-1}$, 20 bar, $H_2/CO_2$ = 4.

(Fig. 3b and Fig. S23). Moreover, the substantial difference in $CO_2$ conversion between direct and indirect conditions further underscores the pivotal role of photo-chemical pathways. As detailed in Table S9, this conversion difference decreased from 36.94% to 20.96% as light intensity increased from 2.8 to 4.8 W $cm^{-2}$, indicating that the relative contribution of hot-carrier effects diminishes at higher irradiances. This decline is likely from elevated reaction temperatures that enhance charge recombination, thereby suppressing the non-thermal effect. Overall, these observations indicate that the non-thermal contribution plays a predominant role in the reaction pathway. By harnessing this effect, the thermal requirement could be substantially reduced while maintaining high catalytic efficiency. In particular, with an external temperature of only 250 °C and a light intensity of 4.0 W $cm^{-2}$, the K–$Fe_{10}Mn_1$ catalyst achieved high $CO_2$ conversion compared to other conventional catalysts in thermal $CO_2$-FTS reaction (Table S11); underscoring the synergistic effect of light and heat in photothermal catalysis, which could compensate for reduced heat input and thus enable energy-efficient operation.

Phase analysis of the spent catalysts under both direct and indirect illumination conditions is presented in Fig. S24. Notably, identical phase compositions were observed regardless of illumination, indicating that light exposure does not induce detectable structural changes in the catalyst.

Furthermore, a comparison of product selectivity at similar $CO_2$ conversion levels, achieved under direct illumination at 3.4 W $cm^{-2}$ and indirect illumination at 4.0 W $cm^{-2}$, revealed no significant differences in product distribution. These findings suggest that light irradiation does not alter the hydrocarbon selectivity, thereby implying that the reaction follows the same mechanistic pathway under both photothermal and purely thermal conditions.

To gain mechanistic insights into the light-induced $CO_2$ hydrogenation over the K-promoted $Fe_{10}Mn_1$ catalyst, we performed *in situ* diffuse reflectance infrared Fourier transform spectroscopy (*in situ* DRIFTS) under both dark and illuminated conditions at 10 bar. The experimental procedure is illustrated in Fig. S25. Fig. 4a presents the IR spectra collected under light irradiation in a $H_2/CO_2$ (4 : 1) mixture, with temperature ramping from ambient to 250 °C, capturing the activation and progression of the photothermal $CO_2$ hydrogenation reaction. At low temperatures, characteristic bands assigned to surface bicarbonate ($HCO_3^-$, 1624 $cm^{-1}$) and bidentate carbonate ($b$-$CO_3^{2-}$, 1285 $cm^{-1}$) were observed, indicating that $CO_2$ adsorption on the catalyst surface is the initial step.[60,61] As the temperature increased, the intensities of these bicarbonate/

Open Access Article. Published on 16 February 2026. Downloaded on 2/25/2026 3:21:28 AM.
This article is licensed under a Creative Commons Attribution 3.0 Unported Licence.

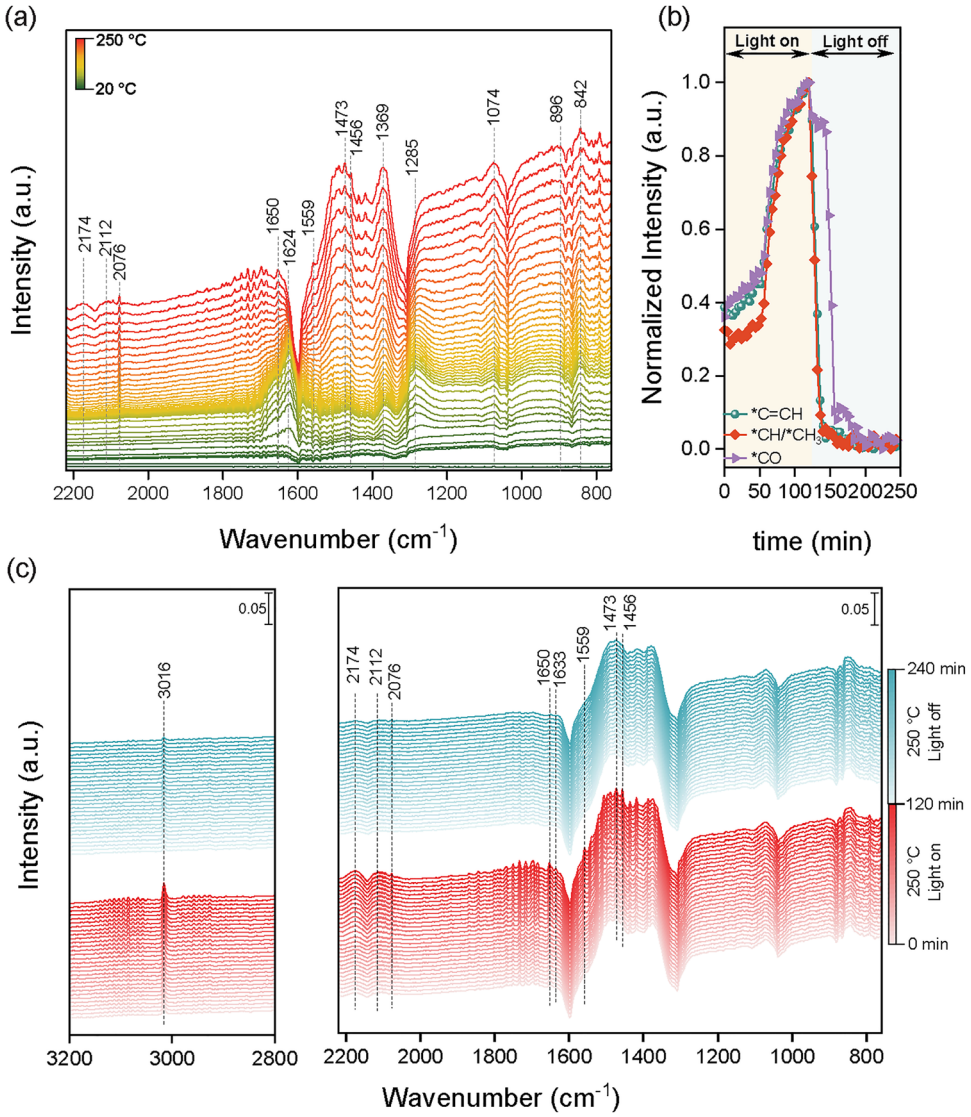


Fig. 4 *In situ* DRIFTS experiments. (a) *In situ* DRIFTS spectra of K–$Fe_{10}Mn_1$ catalyst under $H_2$ and $CO_2$ (4 : 1) at 10 bar with increased temperature from room temperature to 250 °C under light illumination. (b) IR peak intensities of *CH/*$CH_3$, CO*, and *C═CH species as a function of time under light and dark conditions at 250 °C. (c) *In situ* DRIFTS spectra of K–$Fe_{10}Mn_1$ catalyst under $H_2$ and $CO_2$ (4 : 1) at 10 bar and 250 °C upon light and dark illumination.

carbonate species diminished, accompanied by the emergence of vibrational bands corresponding to formate intermediates (HCOO*, 1559 and 1369 $cm^{-1}$)[62,63] and adsorbed CO species (*CO, 2076 $cm^{-1}$),[64,65] signifying the onset of the RWGS reaction. Further temperature elevation led to an increase in the intensity of formate and *CO signals, alongside the appearance of gaseous CO (2174 and 2112 $cm^{-1}$),[66] reflecting enhanced RWGS activity. Simultaneously, hydrocarbon-related bands were detected at around 220 °C, including *C═CH (1650, 1624, and 842 $cm^{-1}$),[46,67,68] and *C–H (896 $cm^{-1}$),[69] pointing to the formation of hydrocarbon species *via* a Fischer–Tropsch synthesis (FTS) pathway. Additionally, thermally stable polydentate carbonates ($p$-$CO_3^{2-}$) could still be observed until 250 °C, evidenced by bands at 1473, 1456, and 1074 $cm^{-1}$.[26,60] Overall, those findings confirmed the reaction pathway of photothermal $CO_2$ hydrogenation.

To further understand the reaction pathway of $CO_2$ hydrogenation under both light and dark conditions, *in situ* IR spectra were collected at 250 °C and 10 bar for each condition over a 2-hour period. As shown in Fig. 4c, the intensities of key surface species increased steadily under continuous light irradiation, indicating the progressive accumulation of active intermediates. In contrast, upon switching off the light, a marked decrease in all signals was observed, reflecting a rapid decline of these intermediates. Fig. 4b presents the normalized intensities of representative species (*C═CH, *CO, and *CH) as a function of time, clearly demonstrating an abrupt drop in signal intensity when illumination stopped. Importantly, the identical intermediates were detected under both illuminated and dark conditions, indicating that the $CO_2$ hydrogenation reaction pathway remains unchanged. These results suggest that light irradiation primarily enhances the reaction performance by

 © 2026 The Author(s). Published by the Royal Society of Chemistry

Open Access Article. Published on 16 February 2026. Downloaded on 2/25/2026 3:21:28 AM.
This article is licensed under a Creative Commons Attribution 3.0 Unported Licence.

accelerating the formation of reactive intermediates, rather than altering the reaction mechanism. Photocurrent measurements for the reduced K–$Fe_{10}Mn_1$ catalyst further confirmed the photochemical properties. As shown in Fig. S26, the photocurrent intensity increases progressively with higher light intensity, indicating enhanced generation and separation of photogenerated charge carriers. To confirm the origin of the photoactivity and the role of Mn, we conduct additional photocurrent measurements of the K–$Fe_{10}Mn_1$ catalyst and a Mn-free sample (K–Fe). As it can be seen in Fig. S27, the photocurrent intensity decreases upon the introduction of Mn. This observation could be explained by (i) a lower proportion of the photoactive phase ($Fe_3O_4$) and/or (ii) the transfer of photogenerated charges from $Fe_3O_4$ to Mn. To confirm this hypothesis, we performed steady-state photoluminescence (PL) measurements. The results confirmed that, upon Mn incorporation, the PL intensity of K–$Fe_{10}Mn_1$ is markedly reduced compared to monometallic K–Fe, indicating enhanced charge separation and transfer between Fe and Mn. (Fig. S28) Overall, those findings are consistent with observations from the direct/indirect illumination experiments, supporting the idea that light enhances catalytic activity through a predominant non-thermal contribution, in combination with a thermal effect.

## 6. Conclusions

In summary, we developed a series of K–$Fe_xMn_y$ catalysts for the photothermal $CO_2$ hydrogenation to hydrocarbons, systematically elucidating the role of Mn incorporation into Fe-based systems. An optimal Mn content could enhance both hydrocarbon productivity and chain-growth probability, whereas excessive Mn reduced reduction ability and carburization process, suppressing C–C coupling and increasing CO selectivity. The K–$Fe_{10}Mn_1$ catalyst, with a finely tuned Fe/Mn ratio, achieved a $C_2^+$ hydrocarbon selectivity of 79.2% and a $C_{2-5}$ yield of 4.8 mmol $g^{-1}$ $h^{-1}$ under 4 W $cm^{-2}$ light irradiation with external heating at 250 °C, 20 bar, and 12 000 mL $g^{-1}$ $h^{-1}$. Mechanistic investigations revealed that non-thermal effects dominate the reaction pathway, accompanied by a minor thermal contribution, enabling exceptional performance under mild conditions. *In situ* DRIFTS further demonstrated that light irradiation could accelerate the formation of key reaction intermediates without altering the fundamental pathway, thereby enhancing overall catalytic efficiency.

## Conflicts of interest

There are no conflicts to declare.

## Data availability

All data supporting the findings of this study are available within the article and its supplementary information (SI). Supplementary information is available. See DOI: https://doi.org/10.1039/d6ey00013d.

Additional datasets and raw characterization files are available from the corresponding authors upon reasonable request.

## Acknowledgements

We gratefully acknowledge the financial support from King Abdullah University of Science and Technology (KAUST).

## References

1 P. Achakulwisut, P. Erickson, C. Guivarch, R. Schaeffer, E. Brutschin and S. Pye, *Nat. Commun.*, 2023, **14**, 5425.
2 D. Zhang, C. Rong, T. Ahmad, H. Xie, H. Zhu, X. Li and T. Wu, *Eng. Rep.*, 2023, **5**, e12584.
3 Q. Hassan, P. Viktor, T. J. Al-Musawi, B. M. Ali, S. Algburi, H. M. Alzoubi, A. K. Al-Jiboory, A. Z. Sameen, H. M. Salman and M. Jaszczur, *Renewable Energy Focus*, 2024, **48**, 100545.
4 I. Overland, J. Juraev and R. Vakulchuk, *Renewable Energy*, 2022, **200**, 379–386.
5 M. Filonchyk, M. P. Peterson, L. Zhang, V. Hurynovich and Y. He, *Sci. Total Environ.*, 2024, **935**, 173359.
6 D. Nong, P. Simshauser and D. B. Nguyen, *Appl. Energy*, 2021, **298**, 117223.
7 N. Mac Dowell, P. S. Fennell, N. Shah and G. C. Maitland, *Nat. Clim. Change*, 2017, **7**, 243–249.
8 P. Gabrielli, M. Gazzani and M. Mazzotti, *Ind. Eng. Chem. Res.*, 2020, **59**, 7033–7045.
9 M. Ahmadi Khoshooei, X. Wang, G. Vitale, F. Formalik, K. O. Kirlikovali, R. Q. Snurr, P. Pereira-Almao and O. K. Farha, *Science*, 2024, **384**, 540–546.
10 X. Wang, E. Toshcheva, A. Rendón-Patiño, C. Martín, U. H. Bhatti, D. Mateo, R. Ahmad, M. H. Alabsi, L. Cavallo and J. M. R. Gallo, *Chem. Eng. J.*, 2025, **507**, 160326.
11 D. Schmider, L. Maier and O. Deutschmann, *Ind. Eng. Chem. Res.*, 2021, **60**, 5792–5805.
12 C. Molinet-Chinaglia, S. Shafiq and P. Serp, *ChemCatChem*, 2024, **16**, e202401213.
13 O. Martin, C. Mondelli, D. Curulla-Ferré, C. Drouilly, R. Hauert and J. Pérez-Ramírez, *ACS Catal.*, 2015, **5**, 5607–5616.
14 O. Martin, A. J. Martín, C. Mondelli, S. Mitchell, T. F. Segawa, R. Hauert, C. Drouilly, D. Curulla-Ferré and J. Pérez-Ramírez, *Angew. Chem.*, 2016, **128**, 6369–6373.
15 T. Pinheiro Araújo, J. Morales-Vidal, T. Zou, M. Agrachev, S. Verstraeten, P. O. Willi, R. N. Grass, G. Jeschke, S. Mitchell and N. López, *Adv. Energy Mater.*, 2023, **13**, 2204122.
16 F. Jiang, B. Liu, S. Geng, Y. Xu and X. Liu, *Catal. Sci. Technol.*, 2018, **8**, 4097–4107.
17 A. Ramirez, L. Gevers, A. Bavykina, S. Ould-Chikh and J. Gascon, *ACS Catal.*, 2018, **8**, 9174–9182.
18 K. Ukoba, K. O. Yoro, O. Eterigho-Ikelegbe, C. Ibegbulam and T.-C. Jen, *Heliyon*, 2024, **10**, e28009.
19 A. O. Maka and J. M. Alabid, *Clean Energy*, 2022, **6**, 476–483.
20 X. Wu, S. Zhang, S. Ning, C. Yang, L. Li, L. Tang, J. Wang, R. Liu, X. Yin and Y. Zhu, *Chem. Sci.*, 2025, **16**, 4568–4594.

Open Access Article. Published on 16 February 2026. Downloaded on 2/25/2026 3:21:28 AM.
This article is licensed under a Creative Commons Attribution 3.0 Unported Licence.

21 S. Luo, X. Ren, H. Lin, H. Song and J. Ye, *Chem. Sci.*, 2021, **12**, 5701–5719.
22 D. Mateo, E. V. Ramos-Fernandez and J. Gascon, *Chem. Catal.*, 2025, **5**, 101569.
23 D. Mateo, J. L. Cerrillo, S. Durini and J. Gascon, *Chem. Soc. Rev.*, 2021, **50**, 2173–2210.
24 C. Song, Z. Wang, Z. Yin, D. Xiao and D. Ma, *Chem. Catal.*, 2022, **2**, 52–83.
25 Y. Li, X. Pei, Z.-J. Wang, L. Shi, H. Song and J. Ye, *ACS Sustainable Chem. Eng.*, 2024, **12**, 17069–17097.
26 B. Deng, H. Song, Q. Wang, J. Hong, S. Song, Y. Zhang, K. Peng, H. Zhang, T. Kako and J. Ye, *Appl. Catal., B*, 2023, **327**, 122471.
27 X. Wang, A. Rendón-Patiño, J. M. R. Gallo, D. Mateo and J. Gascon, *J. Mater. Chem. A*, 2024, **12**, 23541–23550.
28 S. Ning, J. Wang, X. Wu, L. Li, S. Zhang, S. Chen, X. Ren, L. Gao, Y. Hao and C. Lv, *Adv. Funct. Mater.*, 2024, 2400798.
29 S. Ning, X. Wu, H. Song, X. Ma, S. Yue, S. Zhang, L. Tang, R. Liu, X. Yin and S. Ouyang, *J. Am. Chem. Soc.*, 2025, **148**, 1728–1740.
30 J. Zhao, R. Shi, G. I. Waterhouse and T. Zhang, *Nano Energy*, 2022, **102**, 107650.
31 L. Krausser, Q. Yang and E. V. Kondratenko, *ChemCatChem*, 2024, **16**, e202301716.
32 B. Yao, T. Xiao, O. A. Makgae, X. Jie, S. Gonzalez-Cortes, S. Guan, A. I. Kirkland, J. R. Dilworth, H. A. Al-Megren and S. M. Alshihri, *Nat. Commun.*, 2020, **11**, 6395.
33 J. Wei, Q. Ge, R. Yao, Z. Wen, C. Fang, L. Guo, H. Xu and J. Sun, *Nat. Commun.*, 2017, **8**, 15174.
34 K. Zhu, X. Liu, H. Tang, S. Tian, J. Xie, L. Zeng, T. Wang, H. Li, M. Wang and D. Ma, *ACS Catal.*, 2024, **15**, 800–808.
35 J. Zhu, P. Wang, X. Zhang, G. Zhang, R. Li, W. Li, T. P. Senftle, W. Liu, J. Wang and Y. Wang, *Sci. Adv.*, 2022, **8**, eabm3629.
36 J. Wei, R. Yao, Y. Han, Q. Ge and J. Sun, *Chem. Soc. Rev.*, 2021, **50**, 10764–10805.
37 R.-P. Ye, J. Ding, W. Gong, M. D. Argyle, Q. Zhong, Y. Wang, C. K. Russell, Z. Xu, A. G. Russell and Q. Li, *Nat. Commun.*, 2019, **10**, 5698.
38 Y. Zhang, C. Cao, C. Zhang, Z. Zhang, X. Liu, Z. Yang, M. Zhu, B. Meng, J. Xu and Y.-F. Han, *J. Catal.*, 2019, **378**, 51–62.
39 W. Yoon, H. Jo, S. Ahmed, M. K. Khan, M. Irshad, J. Lee, S. S. Bibi and J. Kim, *Chem. Eng. J.*, 2024, **495**, 153617.
40 Y. Han, C. Fang, X. Ji, J. Wei, Q. Ge and J. Sun, *ACS Catal.*, 2020, **10**, 12098–12108.
41 A. S. Skrypnik, S. A. Petrov, V. A. Kondratenko, Q. Yang, A. A. Matvienko and E. V. Kondratenko, *J. Catal.*, 2023, **425**, 286–295.
42 Q. Yang, V. A. Kondratenko, S. A. Petrov, D. E. Doronkin, E. Saraçi, H. Lund, A. Arinchtein, R. Kraehnert, A. S. Skrypnik and A. A. Matvienko, *Angew. Chem., Int. Ed.*, 2022, **61**, e202116517.
43 N. Liu, Q. Fan, J. Wei, G. Zhang, J. Sun, W. Li, C. Song and X. Guo, *ACS Catal.*, 2024, **15**, 179–192.
44 L. Zhang, Y. Dang, X. Zhou, P. Gao, A. P. van Bavel, H. Wang, S. Li, L. Shi, Y. Yang and E. I. Vovk, *Innovation*, 2021, **2**, 100170.
45 P. Sai Prasad, J. W. Bae, K.-W. Jun and K.-W. Lee, *Catal. Surv. Asia*, 2008, **12**, 170–183.
46 H. Ren, H. Yang, J. Xin, C. Wu, H. Wang, J. Zhang, X. Bu, G. Yang, J. Li and Y. Sun, *Appl. Catal. B*, 2024, **358**, 124440.
47 Q. Yang, E. A. Fedorova, D.-B. Cao, E. Saraçi, V. A. Kondratenko, C. R. Kreyenschulte, H. Lund, S. Bartling, J. Weiß and D. E. Doronkin, *Nat. Catal.*, 2025, 1–12.
48 K. Wang, Z. Li, T. Liu, W. Gao, T. Yang, K. Liu, X. Gao, Q. Ma, J. Zhang and T. Zhao, *ACS Catal.*, 2024, **14**, 17469–17479.
49 L. Guo, J. Li, Y. Cui, R. Kosol, Y. Zeng, G. Liu, J. Wu, T. Zhao, G. Yang and L. Shao, *Chem. Commun.*, 2020, **56**, 9372–9375.
50 Z. Yang, Z. Zhang, Y. Liu, X. Ding, J. Zhang, J. Xu and Y. Han, *Appl. Catal., B*, 2021, **285**, 119815.
51 B. Shi, Z. Zhang, Y. Liu, J. Su, X. Liu, X. Li, J. Wang, M. Zhu, Z. Yang and J. Xu, *J. Catal.*, 2020, **381**, 150–162.
52 B. Chen, B. Wu, L. Yu, M. Crocker and C. Shi, *ACS Catal.*, 2020, **10**, 6176–6187.
53 X. Ding, M. Zhu, Y.-F. Han and Z. Yang, *J. Catal.*, 2023, **417**, 213–225.
54 G. Maiti, R. Malessa, U. Löchner, H. Papp and M. Baerns, *Appl. Catal.*, 1985, **16**, 215–225.
55 R. W. Dorner, D. R. Hardy, F. W. Williams and H. D. Willauer, *Catal. Commun.*, 2011, **15**, 88–92.
56 L. Tang, L. He, Y. Wang, B. Chen, W. Xu, X. Duan and A.-H. Lu, *Appl. Catal., B*, 2021, **284**, 119753.
57 D. Ye, W. Tang, T. Zhang, L. Lv, Z. Zou, R. K. Gupta and S. Tang, *Colloids Surf., A*, 2022, **654**, 130145.
58 X. Li, H. O. Everitt and J. Liu, *Nano Res.*, 2019, **12**, 1906–1911.
59 M. J. Landry, A. Gellé, B. Y. Meng, C. J. Barrett and A. Moores, *ACS Catal.*, 2017, **7**, 6128–6133.
60 K. Pokrovski, K. T. Jung and A. T. Bell, *Langmuir*, 2001, **17**, 4297–4303.
61 E.-M. Köck, M. Kogler, T. Bielz, B. Klötzer and S. Penner, *J. Phys. Chem. C*, 2013, **117**, 17666.
62 T. Tagawa, N. Nomura, M. Shimakage and S. Goto, *Res. Chem. Intermed.*, 1995, **21**, 193–202.
63 M.-Y. He, J. White and J. Ekerdt, *J. Mol. Catal.*, 1985, **30**, 415–430.
64 B. Yan, B. Zhao, S. Kattel, Q. Wu, S. Yao, D. Su and J. G. Chen, *J. Catal.*, 2019, **374**, 60–71.
65 G. Blyholder, *J. Phys. Chem.*, 1964, **68**, 2772–2777.
66 F. C. Meunier, *Catal. Today*, 2023, **423**, 113863.
67 S. Ning, J. Wang, X. Wu, L. Li, S. Zhang, S. Chen, X. Ren, L. Gao, Y. Hao and C. Lv, *Adv. Funct. Mater.*, 2024, **34**, 2400798.
68 M. Gao, H. Li, J. Yu, M. Ye and Z. Liu, *AIChE J.*, 2023, **69**, e17881.
69 A. Lagutschenkov, A. Springer, U. J. Lorenz, P. Maitre and O. Dopfer, *J. Phys. Chem. A*, 2010, **114**, 2073–2079.

 © 2026 The Author(s). Published by the Royal Society of Chemistry